# Numerical simulation of M$_2$ internal tides in the South Brazil Bight and their interaction with the Brazil Current

A. F. Pereira,[1] B. M. Castro,[1] L. Calado,[1] and I. C. A. da Silveira[1]

[1] A fully three-dimensional nonlinear primitive equation ocean model is applied to study the semidiurnal internal tide in the South Brazil Bight under summer conditions. Along the shelf break and upper slope of this region, the upper layer (0–600 m) is occupied by the southward flowing Brazil Current. Several numerical experiments were conducted to investigate the generation and propagation of the M$_2$ internal tide. Using horizontally homogeneous and vertically stratified density fields, internal tides were generated over the whole Bight with a clear signal on the continental shelf. When a more realistic summer stratification was considered, a baroclinic jet, representative of the Brazil Current, developed and comparisons between current observations and modeled results were improved. This jet acts as a barrier to the coastward propagation of the internal tide generated over the slope, reflecting it back towards the open ocean. On the negative relative vorticity side of the Brazil Current, located over the shelf, internal tides are trapped, enhancing vertical current variability and, hence, tidally induced mixing. The results highlight the importance of considering background flows when investigating internal tides in regions of strong along-slope baroclinic flows such as western boundary currents.

Citation: Pereira, A. F., B. M. Castro, L. Calado, and I. C. A. da Silveira (2007), Numerical simulation of M$_2$ internal tides in the South Brazil Bight and their interaction with the Brazil Current, *J. Geophys. Res.*, *112*, C04009, doi:10.1029/2006JC003673.

## 1. Introduction

[2] Internal tides have been observed on many continental margins [*Huthnance*, 1989] and hence, shelf slope and adjacent shelf sea regions have been recognised as areas influenced by them [*Wunsch*, 1975]. Early attempts to model the generation and propagation of these internal waves such as, for example, *Rattray et al.* [1969], *Sandstrom* [1976], and *Baines* [1973, 1982], used analytical models with idealized topography and stratification. More recently, several authors have employed primitive equation three-dimensional ocean models to examine internal tides and their interaction with shelf break topography [e.g., *Cummins and Oey*, 1997; *Holloway*, 2001; *Xing and Davies*, 1998]. Thus, the link between the observations of such waves, and the theory of their generation, propagation and structure, is now well established [e.g., *Baines*, 1982; *Gerkema*, 1996].

[3] Internal tides increase shear in the water column, possibly leading to enhanced dissipation and mixing. Internal tides generated by strong tide-topography interactions occasionally break, causing intense turbulent mixing [*Polzin et al.*, 1997; *Ledwell et al.*, 2000]. Turbulent mixing may also be induced far from wave generation sites, because propagating internal tides can interact nonlinearly with background internal waves and cascade part of their energy down to small scales where breaking may occur. Because they can contribute significantly to deep ocean mixing, it is widely recognized that these internal waves play a significant role in global thermohaline circulation [*Munk and Wunsch*, 1998]. Beyond that, due to increased mixing, particularly near the seabed where current shear may be large, they can be important for sediment transport [e.g., *Puig et al.*, 2004] and enhance biological productivity by mixing nutrients vertically into the photic zone [e.g., *Pereira et al.*, 2005].

[4] The southeastern Brazilian continental shelf, in what is known as the South Brazil Bight (SBB), lies between Cabo Frio (23°S) and Cabo Santa Marta (28°40′S) [*Castro and Miranda*, 1998]. The bight has a crescent shape, being widest in the central part (240 km) and narrowest in the proximity of its southwestern and northeastern boundaries (about 50 km). The topography is generally smooth, with isobaths lying parallel to the coastline (Figure 1). The depth of the shelf break varies between 120 and 180 m. The first evidence of the existence of internal tides on the southeast Brazilian continental shelf was documented by *Pereira and Castro* [2007] who used data from three moorings located over the continental shelf near Cabo Frio and a regional numerical model to investigate their generation and propagation. Along this region and as part of the South Atlantic subtropical gyre, the Brazil Current (BC) flows southward near the shelf edge, transporting Tropical Water (T > 20°C and S > 36.6 [*Miranda*, 1982]) and South Atlantic Central Water (10.7°C < T < 20°C and 35.0 < S < 36.4 [*Miranda*,

---

[1]Departamento de Oceanografia Física, Química e Geológica, Instituto Oceanográfico, Universidade de São Paulo, São Paulo, Brazil.
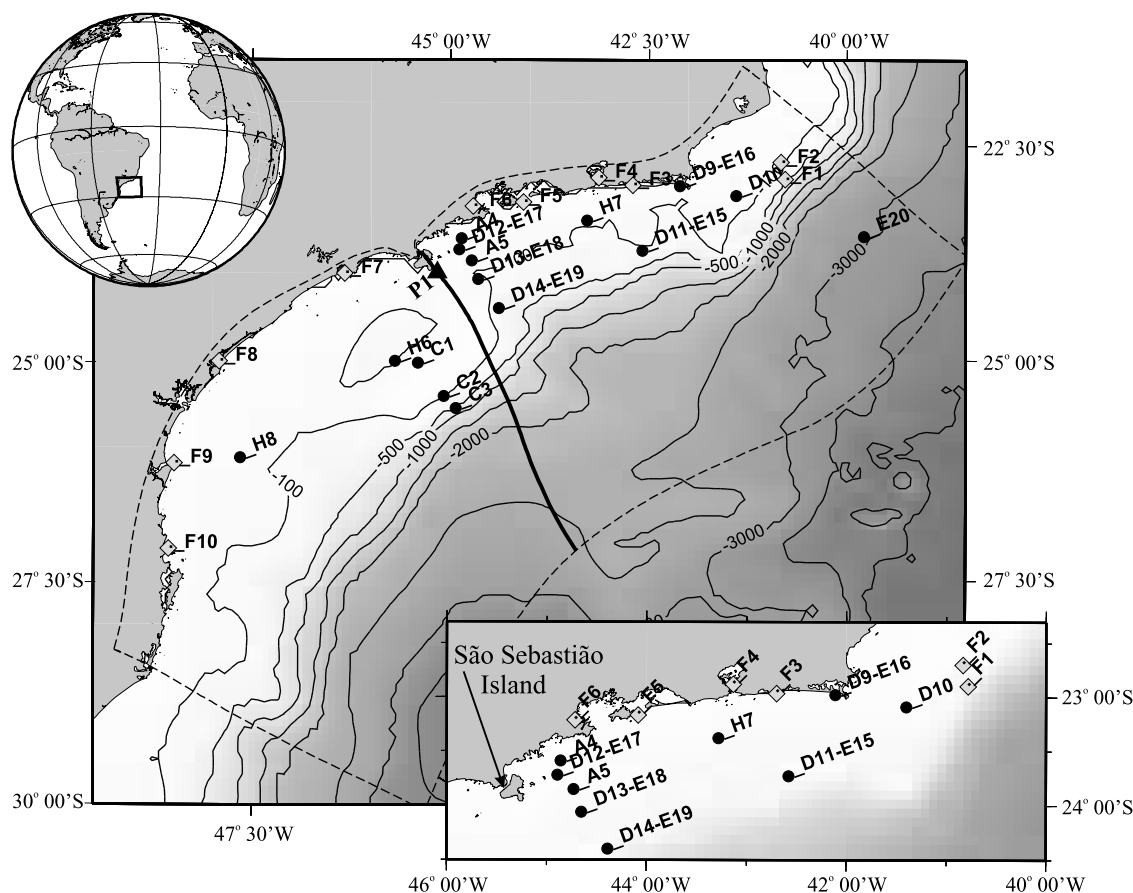
**Figure 1.** Map of the South Brazil Bight, showing bottom topography (m). The dashed lines indicate the model boundaries. The thick solid line identifies the position of the cross-shelf slice for which model results are presented in the following figures. The black triangle, P1, marks the position of the modeled data contoured in Figure 9. Tide gauge positions are indicated by gray diamonds (details in Table 2). Location of each current meter used for comparison is indicated by a black circle (details in Table 3). The small map in the right bottom corner is an enlargement of the northern shelf of the SBB, showing current meter/tidal gauge positions.

1982]) in the upper 500m of the water column. The BC is highly baroclinic and the shallowest of the subtropical western boundary currents in the world ocean. Its transport ranges from 5–10 Sv (1 Sv = $10^6$ m$^3$s$^{-1}$) [*Silveira et al.*, 2000]. Although instantaneous velocities may attain 0.8 m s$^{-1}$, the climatological values are much lower, in part because the current meanders vigorously in the area [*Silveira et al.*, 2004]. The current core is found at the surface and within the SBB, is usually located near the 300–400 m isobath.

[5] A further step towards a complete understanding of the behaviour of such internal waves in the ocean involves the consideration of how they interact with the mean flow and how this interaction may modify the mixing rates. Regions of strong baroclinic flows, e.g., western boundary currents, can alter significantly the behavior of internal waves, reflecting, trapping or prohibiting their generation [*Mooers*, 1975]. Thus, in the case of the SBB, the along-slope baroclinic current associated with the BC may have profound effects on internal tides. The nature of the inter-

action between tidal and background conditions and the proximity of a location to these interactions may be important for the rate of energy transfer to small scales where oceanic mixing occurs [*van Haren*, 2004]. *Rainville and Pinkel* [2004] have investigated the effects of geostrophic vorticity on internal wave propagation in the vicinity of the Kuroshio Current. Their observational study has suggested that the geostrophic vorticity associated with the Kuroshio acts as a barrier, impeding the seaward propagation of internal waves generated at the shelf break onshore of the Kuroshio front.

[6] In this paper, a three-dimensional numerical model has been employed to investigate the generation and propagation of internal tides along the SBB and how these interact with the flow due to the BC.

## 2. Numerical Model

[7] The numerical simulation was carried out using the Princeton Ocean Model [*Blumberg and Mellor*, 1987],

which solves the three-dimensional, free-surface primitive equations using the hydrostatic and Boussinesq approximations. The model uses a terrain-following, sigma coordinate defined by $\sigma = \frac{z-\eta}{D}$, z being a vertical Cartesian coordinate positive upward, and D the total water depth ($D \equiv H + \eta$ where $H$ is the time-mean water depth and $\eta$ the perturbation sea surface elevation). The tide-generating force for the $M_2$ tidal constituent was included in the model's equations following *Schwiderski* [1980]. The model equations are then given by

$$\frac{\partial UD}{\partial t} + \frac{\partial UUD}{\partial x} + \frac{\partial UVD}{\partial y} + \frac{\partial U\omega}{\partial \sigma} = +fVD - \frac{D}{\overline{\rho}_0}\frac{\partial P'}{\partial x} + \frac{\sigma}{\overline{\rho}_0}\frac{\partial P'}{\partial \sigma}\frac{\partial D}{\partial x}$$
$$-\varphi gD\frac{\partial \eta}{\partial x} + \beta gD\frac{\partial \xi}{\partial x} - r(U - \overline{U})D + F_U,$$

$$\frac{\partial VD}{\partial t} + \frac{\partial VUD}{\partial x} + \frac{\partial VVD}{\partial y} + \frac{\partial V\omega}{\partial \sigma} = -fUD - \frac{D}{\overline{\rho}_0}\frac{\partial P'}{\partial y} + \frac{\sigma}{\overline{\rho}_0}\frac{\partial P'}{\partial \sigma}\frac{\partial D}{\partial y}$$
$$-\varphi gD\frac{\partial \eta}{\partial y} + \beta gD\frac{\partial \xi}{\partial y} - r(V - \overline{V})D + F_V,$$

$$\frac{\partial P'}{\partial \sigma} = -gD(\rho - \rho_0),$$

$$\frac{\partial UD}{\partial x} + \frac{\partial VD}{\partial y} + \frac{\partial \omega}{\partial \sigma} + \frac{\partial \eta}{\partial t} = 0,$$

$$\frac{\partial TD}{\partial t} + \frac{\partial TUD}{\partial x} + \frac{\partial TVD}{\partial y} + \frac{\partial T\omega}{\partial \sigma} = F_T,$$

$$\frac{\partial SD}{\partial t} + \frac{\partial SUD}{\partial x} + \frac{\partial SVD}{\partial y} + \frac{\partial S\omega}{\partial \sigma} = F_S;$$

where $t$ is time, $x$ and $y$ are defined as positive eastward and northward, $U$ and $V$ are the velocity components in directions $x$ and $y$, $\omega$ is the velocity component normal to the $\sigma$ = constant surfaces, $\overline{U}$ and $\overline{v}$ are the depth-averaged components of $U$ and $V$, $f = 2\Omega \sin\phi$ is the Coriolis frequency with $\Omega$ the angular velocity of the Earth's rotation and $\phi$ the latitude, $T$ and $S$ are the potential temperature and salinity, $\rho$ is the water density determined from $T$ and $S$ using the equation of state, $\rho_0$ is the background basic density stratification, $\overline{\rho}_0$ is the reference water density, $P'$ is the pressure perturbation associated with the density deviation from the background stratification, $g$ is the acceleration due to gravity; the factor $\varphi$ accounts for the effect of load tides and is assumed to be 0.9 following *Schwiderski* [1980]; $\xi$ is the equilibrium tidal potential and the factor $\beta$ multiplying $\xi$ is the effective elasticity of Earth, assumed to be 0.69 [*Schwiderski*, 1980]; $r(U - \overline{U})$ and $r(V - \overline{V})$ are the bottom shear stress terms where $r = C (\overline{U}^2 + \overline{V}^2)^{1/2}$ and $C$ is a constant drag coefficient, assumed to be 0.0025; $(F_U, F_V)$ and $(F_T, F_S)$ represent the viscosity and diffusivity terms. A more extensive discussion of the features of the model are given by *Blumberg and Mellor* [1987].

[8] The vertical mixing of momentum, heat, and salt are determined by the Mellor-Yamada level 2.5 turbulence closure scheme [*Mellor and Yamada*, 1982], whereas horizontal eddy viscosity and diffusivity coefficients were determined in accordance with the formulation of *Smagorinsky* [1963].

## 2.1. Model Grid and Bathymetry

[9] Figure 1 shows the region being modeled. The numerical grid is orthogonal curvilinear (Figure 2) and
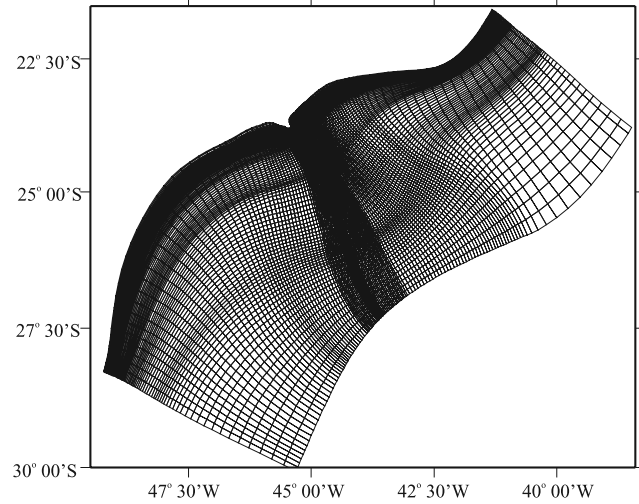


**Figure 2.** Orthogonal grid employed in this study.

has 113 grid points in direction $x$ (NW-SE orientation and almost perpendicular to the shelf break) and 137 grid points in direction $y$ (SW-NE orientation). This grid leads to a variable horizontal resolution: over the continental shelf, the grid spacing varies from 0.2 km to 5 km in the $x$ direction, increasing to between 5 km and 10 km over the continental slope. In depths greater than 2100 m, the resolution perpendicular to the shelf break reaches 35 km. In the $y$ direction, the grid spacing varies from 0.5 km (in the central part of the modeled region) to 35 km near the NE and SW open boundaries. This grid resolves the internal tide wavelength scales ($N_0HT/\pi$, where $N_0$ is the buoyancy frequency, and $T$ the wave period). Assuming typical values of $N_0 = 0.01$ s$^{-1}$ (see Figure 3) and $T = 12.42$ hours for the $M_2$ tidal period, the wavelength varies from around 142 km in water 1000 m deep to 7.1 km in water 50 m deep.

[10] Vertically, the domain is divided into 24 unequally spaced levels ($\sigma = 0$ at the sea surface and $-1$ at the bottom), with logarithmical distribution at the 5 top and 5 bottom layers to gain increased resolution near the surface and near the seabed, according to the distribution: $\sigma = (-1, -0.9958, -0.9916, -0.9833, -0.9666, -0.9333, -0.8666, -0.8, -0.7333, -0.6666, -0.6, -0.5333, -0.4666, -0.4, -0.3333, -0.2666, -0.2, -0.1333, -0.0666, -0.0333, -0.0166, -0.0083, -0.0041, 0)$. A vertical resolution test was made, increasing it to 40 levels (not shown). An intercomparison of results from simulations with 24 and 40 levels showed no essential changes in the radiation pattern of the internal tide. *Cummins and Oey* [1997] arrived at a similar conclusion when simulating $M_2$ internal tides off Northern British Columbia. Another aspect related to the vertical resolution is the pressure gradient error associated with the $\sigma$-coordinate. The use of such a transformation in the presence of steeply sloping bottom topography introduces an artificial cross-shelf baroclinic pressure gradient, which, if geostrophically adjusted, will produce a longshore mean flow. *Haney* [1991] and *Cheng* [1992] showed that for a given topography and stratification the pressure gradient is reduced by increasing the
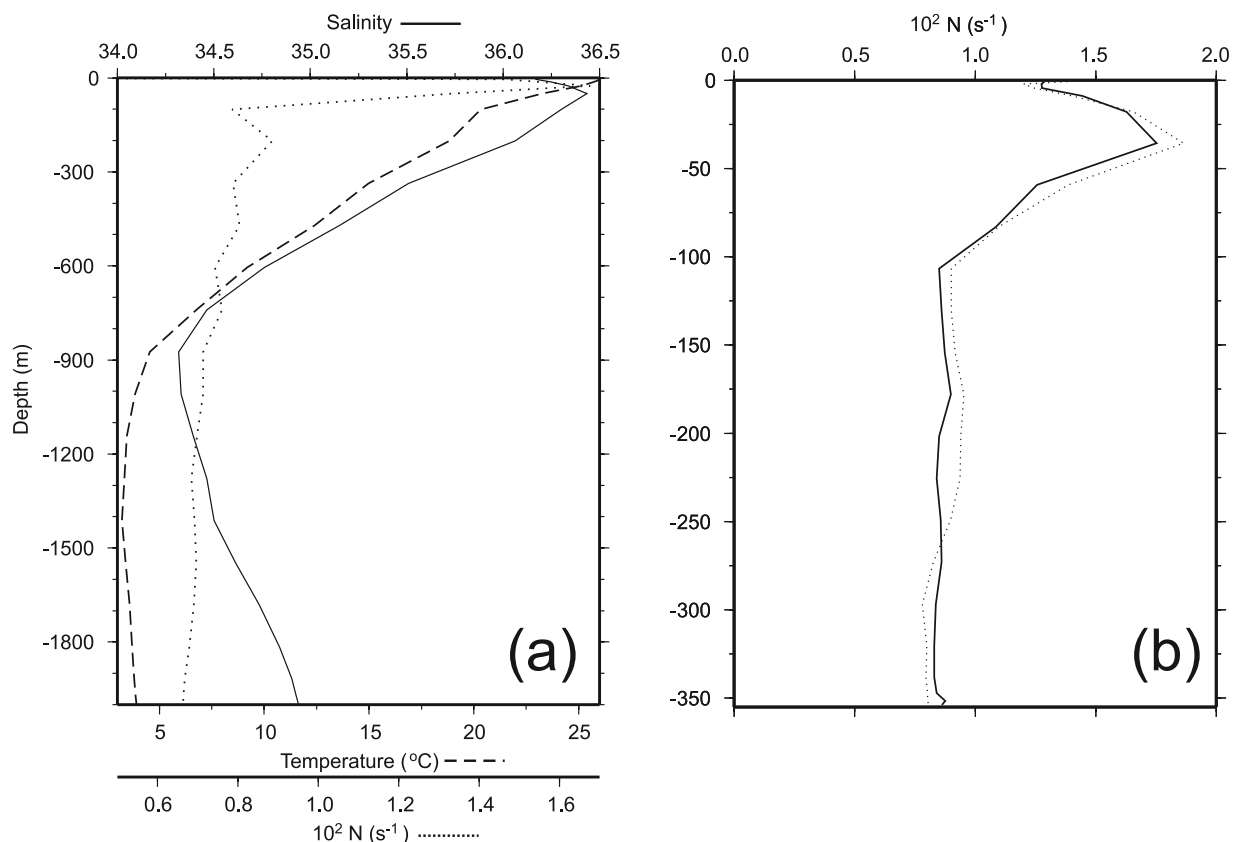
**Figure 3.** (a) Vertical profiles of temperature, salinity and correspondent buoyancy frequency used in the idealized experiment I2. (b) Comparison between buoyancy frequency profiles for a point located on the upper slope for experiments I2 and R3.

vertical resolution. Experiments with no tidal forcing and constant temperature and salinity fields showed that the use of 24 vertical grid levels provides sufficient vertical resolution to reduce the artificial pressure gradient to a level that produces a longshelf geostrophic flow of only $0.5-1.5$ mm s$^{-1}$.

[11] Bottom topography was taken from a high resolution (0.5 to 1 km) topographic database constructed on the basis of digitized nautical charts of the region.

## 2.2. Numerical Experiments, Model Initialization and Boundary Conditions

[12] The numerical experiments of this study are listed in Table 1. The first case, denoted H1, is a control run in which a homogeneous fluid is specified to study the barotropic tides. The baroclinic response of the model was examined by a second experiment, denoted I2. Here temperature and salinity are initialized as horizontally homogeneous and vertically stratified, representative of summer stratification. A typical profile at 2000 m depth was chosen (see Figure 3a) and then a cubic spline interpolation was used to get temperature and salinity data on the sigma levels at each grid point. This was done to remove baroclinic gradients related to the Brazil Current. The last experiment (R3) was conducted to examine the interaction of the internal tides with the along-slope baroclinic flow due to the Brazil Current. In this case, the model is initiated with three-dimensional fields of potential temperature and salinity

representative of summer stratification, taken from a regional climatological hydrography [*Rezende*, 2003]. Figure 3b shows the vertical profile of the buoyancy frequency at a point located at 350 m (i.e., on the slope) for experiments I2 and R3, and Figure 4 illustrates the vertical and horizontal variation of temperature and salinity along the cross-shelf transect, indicated in Figure 1, used in the R3 simulation.

[13] Open boundary conditions for temperature and salinity are different for experiments I2 and R3. When considering an idealized density profile (I2), temperature and salinity fields are held to their initial values over the outer 5 grid points of each open boundary. In the case of experiment R3, each open boundary was treated differently, following *Rezende* [2003]. The NE boundary was considered as inflow while the others were treated as outflow. This was done to guarantee a constant SW flow associated with the temperature and salinity fields set on the NE limit. Along the NE boundary, both variables are relaxed in accordance with the equation:

$$F = \gamma F_b + (1 - \gamma)\tilde{F}$$

where $F$ represents the temperature or the salinity value, $\tilde{F}$ is the variable value at the current timestep, $F_b$ is the variable value prescribed at the open boundary and

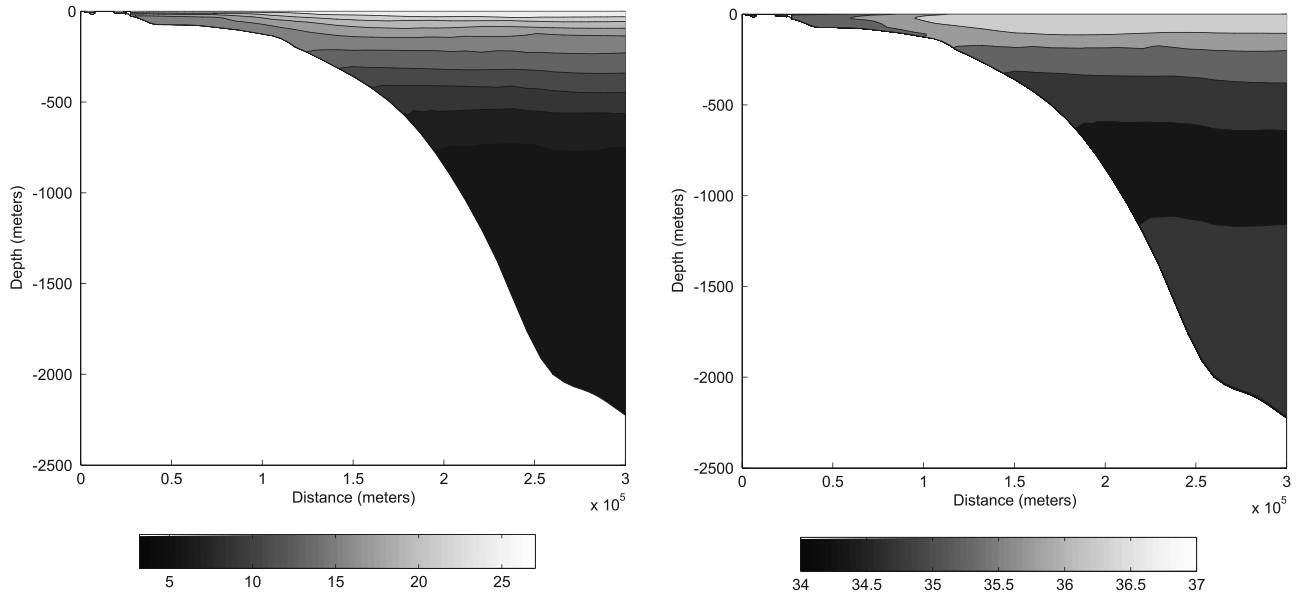$$\gamma = 1 - \tanh[K \times (N - i)], \qquad i = 1, 2, \ldots N.$$

**Figure 4.** Temperature (left, °C) and salinity (right) distribution along cross-shelf slice indicated in Figure 1 as used for model initialization for experiment R3.

[14] N is the number of points being relaxed ($N = 10$), and K is a factor equal to 0.5.

[15] On the SW and SE boundaries, the simplified form of the advection equation was considered:

$$\frac{\partial P}{\partial t} + V_b \frac{\partial P}{\partial s} = 0$$

where P represents temperature or salinity, $V_b$ and $\partial(.)/\partial s$ the velocity component and the derivative normal to the boundary, respectively. This equation was implemented in its finite difference form following *Mellor* [1996]:

$$P_b^{n+1} = P_b^n + r_1\left(P_b^n - P_{b-1}^n\right) + r_2\left(P_e^{n+1} - P_b^n\right)$$
$$r_1 = 0.5(\Delta t_i/\Delta s)\left(V_b^n + |V_b^n|\right)$$
$$r_2 = 0.5(\Delta t_i/\Delta s)\left(V_b^n - |V_b^n|\right)$$

where $\Delta t_i$ is the internal timestep, $\Delta s$ is the grid space normal to the boundary, n is the instant centered in time and $P_e$ is the prescribed temperature or salinity value at the boundary. $P_e$ will only modify the solution in an inflow situation ($V_b < 0 \Rightarrow r_1 = 0$). If $V_b > 0$, $r_2$ is null and the property is advected outwards.

[16] The following descriptions of open boundary conditions are valid for all experiments. Tidal elevations are prescribed at the open boundaries using the global tidal model TPXO.5 [*Egbert and Erofeeva*, 2002]. Only the main semidiurnal tidal constituent $M_2$ is considered.

[17] A zero normal velocity is imposed at the lateral land boundary, while the normal gradient of the tangential velocity component is set to zero at the open boundaries. For the depth-averaged normal velocity, a radiation condition is applied along the open boundaries:

$$\bar{v}_\perp = \bar{v} + \sqrt{\frac{g}{D}}(\eta - \eta_F)$$

where $\bar{v}_\perp$ is the radiated depth mean current (i.e., $\overline{U}$ at southeastern model boundary and $\overline{V}$ at northeastern and southwestern model boundaries), $\eta_F$ is the prescribed elevation, $\bar{v}$ and $\eta$ are the normal component of the barotropic tidal current and the elevation calculated in the current time-step, respectively.

[18] For the baroclinic flow, an implicit Orlanski radiation condition is applied at the open boundary [*Chapman*, 1985]:

$$C_L = \frac{\phi_{b+1}^{n-1} - \phi_{b+1}^{n+1}}{\phi_{b+1}^{n+1} + \phi_{b+1}^{n-1} - 2\phi_{b+2}^n}$$

where $\phi$ represents the baroclinic velocity, and b the grid point at a boundary; $t = n\Delta t$ where t is the time and $\Delta t$ the model time step. Thus, the boundary condition becomes

$$\phi_b^{n+1} = \left[\phi_b^{n-1}(1 - \mu) + 2\mu\phi_{b+1}^n\right]/(1 + \mu)$$

and

$$\mu_i = \begin{cases} 1, & \text{if } C_L \geq 1 \\ C_L, & \text{if } 0 < C_L < 1 \\ 0, & \text{if } C_L \leq 0. \end{cases}$$

## 2.3. Integration Time, Time Stepping, and Harmonic Analysis

[19] The model was integrated for 60 days, beginning from rest, with a time-step of 10 s for the baroclinic mode

**Table 1.** Numerical Experiments Mentioned in This Study

| Experiment | Stratification Profile |
|---|---|
| H1 | none |
| I2 | idealized |
| R3 | realistic |

and 2 s for the barotropic mode. The forcing is gradually increased to its full strength within the first 10 days. Hourly fields of surface elevation and modeled velocities from the last 30 days were subject to a harmonic analysis using the algorithms developed by *Foreman* [1977, 1978].

# 3. Results

## 3.1. M₂ Barotropic Tide

[20] The results in this section are drawn from experiment H1 with homogeneous fluid. The amplitude and phase of the surface elevation field at the $M_2$ frequency are presented in Figure 5. Higher amplitudes (up to 0.4 m) are found near the coast. The $M_2$ phase distribution is influenced by the existence of two amphidromic points located outside the modeled region: one, which is virtual and has clockwise rotation, is located just southward of the coastline (near 33°S [*Egbert and Erofeeva*, 2002]), and a second is situated in the middle of the South Atlantic Ocean basin and rotates counterclockwise [*Egbert and Erofeeva*, 2002]. The first amphidromic point, described above, influences the southern portion of the modeled region, producing cophase lines lying approximately parallel to the coast and increasing in a southeasterly direction. In the northern part of the modeled region, the cophase lines lie perpendicular to the coast, increasing to the south-west, consistent with the existence of the second amphidromic pont in the central part of the South Atlantic Ocean. Around 24°S, the $M_2$ tide presents co-oscillating characteristics (phase lines parallel to the isobaths) and a slight amplification across the shelf.

[21] A comparison is made between modeled and observed $M_2$ tidal elevations and phases at 14 coastal and offshore locations (Table 2). Table 2 also lists the latitudes and the longitudes of the respective locations (see Figure 1) and also the local depths. For a given tide gauge, the closest corresponding model grid point was chosen for comparison. The comparison between the model and observations is close, with an RMS difference in amplitude and phase of 2.88 cm and 10.6°, respectively.

[22] Tidal current ellipses for the depth-averaged velocity are presented in Figure 6 for the $M_2$ constituent. In deeper regions, tidal currents are small, O(1 cm s$^{-1}$). On the shelf located south of 24°S, $M_2$ tidal currents are greater, O(5 cm s$^{-1}$), than those found on the shelf to the north, O(2.5 cm s$^{-1}$). The continental shelf is wider and tidal amplitudes are higher south of 24°S (Figure 5). Consequently, there is a larger tidal prism to be filled across the shelf between low and high water, increasing tidal current speed. Over most of the model domain, tidal ellipses rotate counterclockwise. It is interesting to note the dominant cross-shelf polarization of the ellipses over most of the model domain, which is an essential ingredient for generating internal tides because the stratified fluid is forced more vigorously up and down the continental slope.

[23] Table 3 lists positions, local depths and current meter depths at 20 moorings available for model comparison. The $M_2$ observed barotropic current, defined as the depth-averaged velocity for each location, was compared with modeled results (Tables 4 and 5). The RMS difference in semi-major axis length is 1.17 cm s$^{-1}$, in phase 23° and in orientation 14°. The close agreement between barotropic tidal currents' strength and ellipse orientation is particularly important for attaining accurate forcing of the baroclinic tide.

## 3.2. M₂ Baroclinic Tide

[24] To examine the baroclinic response of the model, results from experiment I2 are considered first.

### 3.2.1. Idealized Case

[25] The barotropic response is nearly unchanged in this run as compared to the unstratified case, H1. However, a vigorous internal tide is generated in I2 that affects the tidal current over much of the domain. The regions of internal tidal influence are delineated in Figure 7, which shows contours of the RMS $M_2$ baroclinic current on a near-surface ($\sigma = -0.00416$) sigma level. Here the baroclinic current is defined as the difference between the total and the depth-averaged current. The RMS of the near-surface baroclinic current gives an indication of the strength of the internal tide. The results of Figure 7 indicate that the internal tidal influence is greatest over the shelf and over the upper and middle slope. Over the shelf, RMS baroclinic values indicate a significant internal tide activity, especially south of São Sebastião Island (see Figure 1) where RMS $M_2$ baroclinic currents can reach 6 cm s$^{-1}$ (standard deviation of 1 cm s$^{-1}$ and 2 cm s$^{-1}$ north and south of São Sebastião Island, respectively). The alternating pattern of high and low tidal currents modeled over the shelf indicates the propagation rays of the internal tide: higher values near the surface occur where the internal tide is reflected by the sea surface. A similar pattern is found near the bottom due to reflection of the internal tide at the bottom (not shown). In deep water (H > 1000 m), RMS $M_2$ currents near the surface have an average value of 1.5 cm s$^{-1}$ with a standard deviation of 0.5 cm s$^{-1}$.

[26] The vertical structure of the internal tide can be seen from a sample cross-section plot over the whole model domain (excluding the flow relaxation zone) of the $M_2$ semi-major axis length of the baroclinic currents (Figure 8). The location of the section is shown in Figure 1. There is clearly a significant internal tide with its strongest motion centered around the top of the continental slope and over the whole continental shelf where baroclinic currents reach 10 cm s$^{-1}$. The time series of temperature and cross-shelf current velocity (total velocity, i.e., barotropic and baroclinic components) for a location placed over the shelf (P1 at Figure 1) along this cross-section are presented in Figure 9. The temperature contours clearly show the semidiurnal internal tide oscillation (Figure 9, left). The velocities (Figure 9, right) show a small tidal phase difference over the water depth and correspond well with the oscillations seen in the time sequence of isothermal depths. The phase relationship between elevations and velocities (seaward mid-depth flow at the peak of the wave) shows the waves to be propagating shoreward.

[27] The internal tide signal is seen to be following the paths of the internal tide characteristics defined as:

$$\alpha^2 = \left[ \frac{\omega^2 - f^2}{N^2(z) - \omega^2} \right], \quad (1)$$

where $\omega$ is the wave frequency and $N(z)$ the depth varying buoyancy frequency. The relationship between topographic slope ($\gamma$) and the characteristics indicates regions of
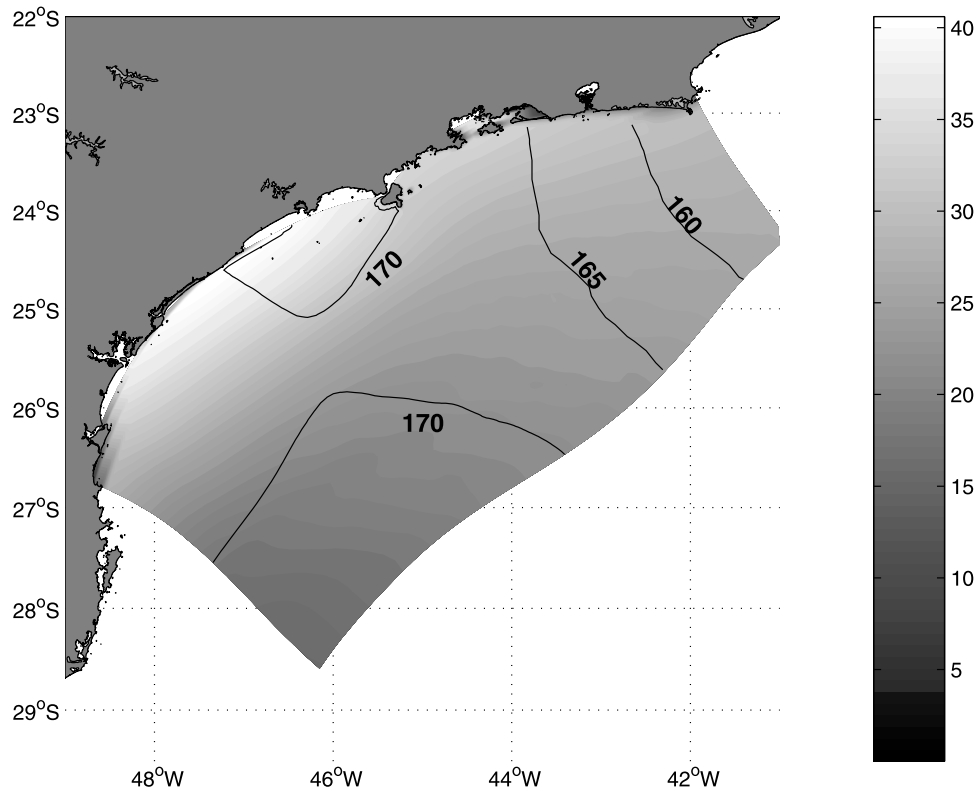
**Figure 5.** Amplitude (cm) and Greenwich phase (degrees) of the calculated surface elevation of the M$_2$ tide. The amplitude is denoted by color shading, the phase by the black contour.

internal tide generation and its propagation [*Baines*, 1982]. Along the sample cross-section (Figure 1) at approximately 1200 m and 1700 m depths (Figure 10, symbols), the slope is critical ($\gamma = \alpha$). Internal tides are not expected to be generated at the lower critical point because the slope is concave [*Azevedo et al.*, 2006]. In depths shallower than 1200 m (upper slope and continental shelf) and deeper than 1700 m (lower slope), the slope is subcritical ($\gamma < \alpha$, Figure 10, symbols). Between 1200 m and 1700 m, the slope is supercritical ($\gamma > \alpha$, Figure 10, symbols) To

exemplify the M$_2$ internal tide propagation, a characteristic trace emanating from the critical point at 1200 m is shown in Figure 11.

[28]  The pattern described above for the ratio $\gamma/\alpha$ is valid for the whole SBB. Comparing the results presented in Figure 8 and the analysis of the linear theory [*Baines*, 1982], it is possible to deduce that the internal tide is seen generated between 600 m and 1400 m where the slope is near-critical for the M$_2$ frequency ($0.7 < \gamma/\alpha < 1.3$ [*Nash et al.*, 2004]), propagating both onshore and offshore.

**Table 2.** Comparison of Observed and Modeled M$_2$ Tidal Amplitude (A, cm) and Greenwich Phase (G, degrees)[a]

| Location | Longitude | Latitude | Water Depth, m | Observed | | Modeled | |
|---|---|---|---|---|---|---|---|
| | | | | A | G | A | G |
| F1 | 40°47′W | 22°54′S | 200 | 31 | 171 | 29 | 150 |
| F2 | 40°50′W | 22°42′S | no data | 32 | 164 | 29 | 149 |
| F3 | 42°42′W | 22°58′S | coast | 29 | 160 | 26 | 161 |
| F4 | 43°08′W | 22°53′S | coast | 33 | 169 | 26 | 163 |
| F5 | 44°05′W | 23°10′S | coast | 25 | 150 | 26 | 166 |
| F6 | 44°43′W | 23°13′S | coast | 33 | 161 | 29 | 166 |
| F7 | 46°20′W | 24°00′S | coast | 35 | 173 | 34 | 172 |
| F8 | 47°55′W | 25°01′S | coast | 36 | 187 | 34 | 166 |
| F9 | 48°29′W | 26°11′S | coast | 31 | 161 | 31 | 160 |
| F10 | 48°33′W | 27°09′S | coast | 22 | 157 | 21 | 161 |
| H6 | 45°42′W | 25°01′S | 92 | 21 | 171 | 24 | 170 |
| H7 | 43°17′W | 23°23′S | 100 | 24 | 167 | 25 | 163 |
| H8 | 47°30′W | 26°18′S | 74 | 24 | 160 | 26 | 166 |

[a]Data from locations F1 to F10 are from *FEMAR* [2000] and H6 to H8 from *Mesquita and Harari* [2003].
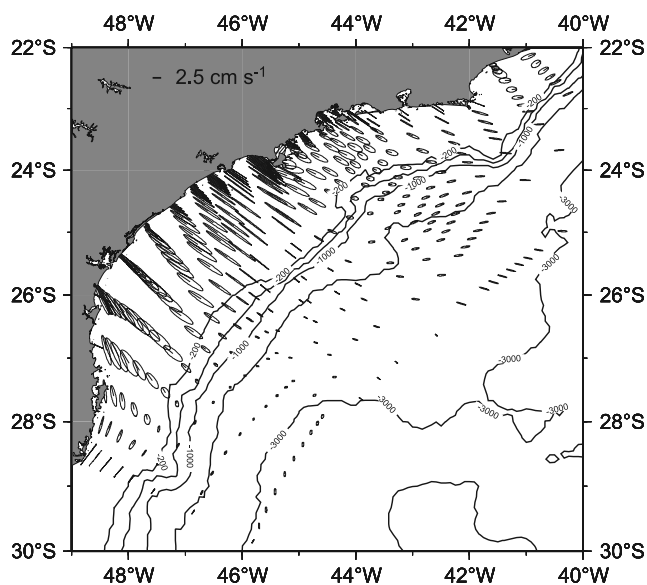
**Figure 6.** Spatial distribution of $M_2$ barotropic tidal ellipses. Solid (dashed) line ellipses rotate counterclockwise (clockwise) and the line from the center indicates the Greenwich phase. Isobaths of 200, 500, 1000, 2000 and 3000 m are plotted.

[29] As will be shown in the next section, such internal wave activity along the slope and continental shelf of the modeled region was not observed in the mooring data available for model comparison.

[30] Figure 12 shows mean values of the vertical eddy diffusivity ($Kd$) at a near-bottom sigma level ($\sigma = -0.9916$).

The mean $Kd$ is presented as the time mean of a 30-day time series and includes the contribution of the bottom friction induced shear due to the barotropic tide. High values of this coefficient (up to $4 \times 10^{-4}$ m$^2$s$^{-1}$) are found over the shelf south of São Sebastião Island (see Figure 1). In this same region, there is an alternating pattern of high and low values of $Kd$. Higher values are found where higher tidal currents were modeled (see Figure 7). The intense internal tide activity modeled over the shelf increases the vertical shear along the water column, resulting in an intense vertical mixing rate. Over the continental slope, $Kd$ values are about $0.5 \times 10^{-4}$ m$^2$s$^{-1}$.

### 3.2.2. Realistic Case

[31] Here the effect of the BC (Figures 13 and 14), an along-slope baroclinic flow, upon the generation and propagation of internal tides, i.e., the interaction between internal tides and background conditions, is investigated.

[32] Modeled data were filtered to separate superinertial frequency (tides) from subinertial frequency motions (BC). Figure 13 shows the RMS values of the baroclinic currents with period greater than 33 hours at $\sigma = -0.00416$. Using the climatological data to initiate this experiment, an along-slope baroclinic flow is produced mainly between the 100 m and 200 m isobaths. Velocities exceed 24 cm s$^{-1}$. The vertical structure of this along-slope flow can be seen in Figure 15. In this snapshot at time = 45 days after initialization, southward currents reach 35 cm s$^{-1}$ and the flow has a v-shape. Near the coast, a northward flow is present. Some noise is noticeable due to internal tide activity. These results are similar to those presented by *Rezende* [2003] who employed the same climatological data set as is used here to investigate the Brazil Current and South Atlantic Central Water intrusions in the SBB. Thus we assume that the climatological BC is well represented by the model.

**Table 3.** Locations for Comparisons Between Modeled and Observed Tidal Currents

| Location | Longitude | Latitude | Water Depth, m | Current Meter Depth, m |
|---|---|---|---|---|
| C1[a] | 45°25′W | 25°02′S | 100 | 30, 58, 91 |
| C2 | 45°05′W | 25°25′S | 200 | 31, 74, 127, 190 |
| C3 | 44°56′W | 25°33′S | 1000 | 29, 91, 293, 698 |
| A4[b] | 44°52′W | 23°36′S | 45 | 12 |
| A5 | 44°44′W | 23°51′S | 75 | 12, 36, 60 |
| H6[c] | 45°42′W | 25°01′S | 92 | 5, 15, 30, 40 |
| H7 | 43°17′W | 23°23′S | 100 | 0, 10, 20, 30, 40, 50, 60, 70, 80, 90 |
| H8 | 47°39′W | 26°07′S | 65 | 5, 10, 20, 30, 40, 50, 60 |
| D9[d] | 42°06′W | 22°59′S | 50 | 49 |
| D10 | 41°24′W | 23° 05′S | 100 | 75, 94 |
| D11 | 42°35′W | 23°44′S | 200 | 23, 85, 155, 194 |
| D12 | 44°54′W | 23°44′S | 51 | 10, 30 |
| D13 | 44°39′W | 24°04′S | 100 | 23, 75 |
| D14 | 44°23′W | 24°24′S | 200 | 23, 85, 155, 194 |
| E15[e] | 42°34′W | 23°43′S | 200 | 23, 85, 155, 194 |
| E16 | 42°07′W | 22°59′S | 50 | 44 |
| E17 | 44°54′W | 23°44′S | 50 | 10, 30 |
| E18 | 44°38′W | 24°04′S | 100 | 23 |
| E19 | 44°22′W | 24°23′S | 200 | 85, 155, 194 |
| E20 | 39°47′W | 23°34′S | 3000 | 800, 1200, 1800, 2200 |

[a]Data indicated as C* are from *Moreira* [1997].
[b]Data indicated as A* are from *Alves* [1992].
[c]Data indicated as H* are from *Mesquita and Harari* [2003].
[d]All locations indicated as D* refer to unpublished data from the Laboratório de Hidrodinâmica Costeira (LHiCo, Instituto Oceanográfico) that were collected between December 2001 and March 2002.
[e]All locations indicated as E* refer to unpublished data from the Laboratório de Hidrodinâmica Costeira (LHiCo, Instituto Oceanográfico) that were collected between January 2003 and April 2003.

**Table 4.** Comparison of Observed and Computed Semimajor Axis $A$ (cm s$^{-1}$), Inclination $\theta$ (degrees) and Direction of Rotation $R$ (Positive, Counterclockwise) of the M$_2$ Current Ellipse at Locations Described in Table 3[a]

| Site and Depth | Observed A | θ | R | Calc H1 A | θ | R | Calc I2 A | θ | R | Calc R3 A | θ | R |
|---|---|---|---|---|---|---|---|---|---|---|---|---|
| C1 30 | 4.9 | 162 | + | 5.2 | 147 | + | 5.8 | 142 | + | 5.3 | 152 | + |
| 58 | 5.4 | 159 | + | | | | 6.5 | 142 | + | 5.4 | 152 | + |
| 91 | 5.5 | 157 | + | | | | 6.5 | 142 | + | 5.4 | 152 | + |
| C2 31 | 2.5 | 164 | + | 3.0 | 153 | + | 4.0 | 143 | + | 2.5 | 154 | + |
| 74 | 2.7 | 169 | + | | | | 3.7 | 142 | + | 2.7 | 153 | + |
| 127 | 2.6 | 177 | + | | | | 3.6 | 142 | + | 3.5 | 153 | + |
| 190 | 4.2 | 131 | + | | | | 3.5 | 142 | + | 3.6 | 133 | + |
| C3 29 | 2.6 | 43 | + | 1.0 | 116 | + | 2.7 | 38 | + | 0.8 | 44 | + |
| 91 | 2.7 | 110 | + | | | | 1.0 | 123 | + | 1.3 | 124 | + |
| 293 | 1.3 | 172 | + | | | | 0.4 | 166 | + | 1.3 | 164 | + |
| 698 | 1.6 | 131 | − | | | | 2.6 | 141 | + | 0.9 | 143 | + |
| A4 12 | 1.2 | 172 | + | 2.1 | 162 | + | 1.7 | 152 | + | 2.0 | 152 | + |
| A5 12 | 2.4 | 113 | + | 2.9 | 120 | + | 4.7 | 130 | + | 2.7 | 134 | + |
| 36 | 2.6 | 110 | + | | | | 3.8 | 133 | + | 3.0 | 134 | + |
| 60 | 2.3 | 123 | + | | | | 2.4 | 132 | + | 2.9 | 133 | + |
| H6 5 | 6.0 | 156 | − | 5.5 | 141 | + | 4.0 | 142 | − | 5.5 | 152 | − |
| 15 | 5.2 | 163 | − | | | | 4.4 | 142 | + | 5.4 | 161 | − |
| 30 | 4.5 | 115 | − | | | | 5.6 | 141 | + | 5.6 | 142 | − |
| 40 | 4.4 | 115 | − | | | | 6.6 | 141 | + | 5.7 | 142 | − |
| H7 5 | 1.3 | 71 | − | 1.9 | 85 | + | 1.8 | 147 | + | 1.7 | 154 | − |
| 10 | 2.4 | 150 | + | | | | 1.8 | 147 | + | 1.8 | 154 | + |
| 20 | 2.0 | 8 | + | | | | 1.9 | 148 | + | 1.9 | 154 | + |
| 30 | 2.0 | 10 | − | | | | 1.9 | 147 | + | 2.0 | 153 | − |
| 40 | 1.6 | 6 | + | | | | 2.0 | 147 | + | 1.9 | 153 | + |
| 50 | 2.1 | 162 | − | | | | 2.1 | 148 | + | 1.9 | 153 | + |
| 60 | 2.3 | 170 | − | | | | 2.1 | 147 | + | 2.0 | 153 | − |
| 70 | 1.8 | 75 | − | | | | 2.1 | 147 | + | 2.0 | 153 | − |
| 80 | 2.4 | 149 | − | | | | 2.2 | 147 | + | 2.1 | 153 | − |
| 90 | 2.3 | 48 | − | | | | 2.2 | 147 | + | 2.1 | 153 | − |
| H8 5 | 7.3 | 115 | − | 4.8 | 139 | + | 4.4 | 130 | + | 4.7 | 129 | − |
| 10 | 7.0 | 121 | − | | | | 4.5 | 131 | + | 4.7 | 129 | − |
| 20 | 7.5 | 126 | − | | | | 4.9 | 132 | + | 4.9 | 129 | − |
| 30 | 6.6 | 129 | − | | | | 5.4 | 130 | + | 5.0 | 129 | − |
| 40 | 5.1 | 123 | + | | | | 5.8 | 131 | + | 5.1 | 128 | + |
| 50 | 45.9 | 131 | − | | | | 6.1 | 132 | + | 5.0 | 138 | + |
| 60 | 7.6 | 125 | − | | | | 6.6 | 134 | + | 5.1 | 140 | − |
| D10 75 | 2.1 | 102 | − | 2.6 | 75 | + | 1.5 | 108 | + | 2.6 | 103 | − |
| 94 | 2.4 | 48 | − | | | | 1.5 | 108 | + | 2.4 | 103 | − |

[a]For experiment H1, listed values refer to depth-averaged values.

[33] High-passed filtered RMS baroclinic currents at $\sigma = -0.00416$ are shown in Figure 14. It is evident that internal tide activity is greatly reduced in this experiment as compared to that of the idealized experiment (see Figure 7). RMS baroclinic velocities are about half of those obtained by the idealized I2 calculation, and regions of internal tide influence are reduced. Much of the internal tide activity is found over the shelf located southward of São Sebastião Island. Over the slope, below 500 m, very little, if any, influence is modeled. In this calculation, average high-passed baroclinic currents near the surface are about 1 and 1.5–2.0 cm s$^{-1}$ (standard deviation of 0.05 cm s$^{-1}$ and 0.3–0.8 cm s$^{-1}$) in the deep ocean and on the shelf, respectively.

[34] The vertical distribution of the M$_2$ semi-major axis length of the baroclinic current (Figure 16) along the sample cross-section (see Figure 1) exhibits a region of enhanced surface velocities (up to 2 cm s$^{-1}$) in the areas where the BC lateral boundaries are located (see Figure 15). When these results are compared with those from experiment I2 (Figure 8), it is clear that, over the shelf and slope, M$_2$ baroclinic currents and internal tide activity are greatly reduced even though the ratio $\gamma/\alpha$ for this calculation is basically the same at the bottom as that given by calculation I2 (Figure 10). The ratio for experiments R3 and I2 differ only on the shelf near the coast where $\gamma/\alpha$ is supercritical for R3 and subcritical for I2. They also present a small difference close to the lateral boundaries of the BC but, even so, the subcritical condition is maintained for both calculations.

[35] A comparison of observed and computed M$_2$ ellipse parameters at a number of current meter sites (see Table 3) is presented in Tables 4 and 5. These results correspond to the total velocity, i.e., the solution including both barotropic and baroclinic components were harmonically analyzed together. Tables 4 and 5 present results from calculations I2 and R3. Observations from moorings E15 to E20 were compared to the same model results used for comparison with data collected at moorings D9-D14 (see Table 3 for details). The differences between observed tidal currents at the same depth and location but at different period (the case of moorings D9-14 and E15-19) are evident. If the nature of internal tides is dependent on the stratification, it is to be expected that tidal currents at the same depth and location will vary on timescales commensurate with the variability of the stratification.

[36] There is a slight improvement in the computed semimajor axis and direction of rotation of the ellipse in experiment R3 as compared with the results of I2 (see

**Table 5.** Comparison of Observed and Computed Semimajor Axis $A$ (cm s$^{-1}$), Inclination $\theta$ (degrees) and Direction of Rotation $R$ (Positive, Counterclockwise) of the M$_2$ Current Ellipse at Locations Described in Table 3[a]

| Site and Depth | Observed A | θ | R | Calc H1 A | θ | R | Calc I2 A | θ | R | Calc R3 A | θ | R |
|---|---|---|---|---|---|---|---|---|---|---|---|---|
| D11 23 | 3.5 | 56 | + | 1.8 | 65 | + | 2.0 | 149 | + | 3.5 | 155 | + |
| 85 | 3.6 | 100 | + | | | | 1.6 | 150 | + | 1.4 | 168 | + |
| 155 | 4.2 | 54 | − | | | | 1.6 | 149 | + | 1.2 | 168 | + |
| 194 | 4.0 | 50 | − | | | | 1.6 | 148 | + | 1.0 | 170 | − |
| D12 10 | 3.7 | 18 | − | 2.4 | 82 | + | 3.4 | 154 | + | 2.1 | 146 | − |
| 30 | 2.6 | 154 | − | | | | 3.2 | 152 | + | 2.8 | 154 | − |
| D13 23 | 3.4 | 150 | − | 3.0 | 89 | + | 3.4 | 142 | + | 3.3 | 151 | − |
| 75 | 3.5 | 177 | − | | | | 5.0 | 155 | + | 2.8 | 157 | − |
| D14 23 | 3.4 | 176 | − | 2.1 | 52 | + | 2.6 | 154 | + | 2.8 | 155 | − |
| 85 | 3.7 | 27 | − | | | | 2.8 | 150 | + | 1.9 | 152 | − |
| 155 | 2.9 | 9 | − | | | | 3.0 | 150 | + | 1.8 | 150 | − |
| 194 | 3.6 | 13 | − | | | | 3.3 | 153 | + | 1.8 | 152 | − |
| E15 23 | 1.8 | 22 | − | 1.8 | 95 | + | 2.0 | 149 | + | 3.5 | 155 | + |
| 85 | 3.9 | 85 | − | | | | 1.6 | 150 | + | 1.4 | 168 | + |
| 155 | 1.7 | 104 | + | | | | 1.6 | 149 | + | 1.2 | 168 | + |
| 194 | 0.3 | 162 | − | | | | 1.6 | 148 | + | 1.0 | 170 | − |
| E16 44 | 1.8 | 121 | − | 2.3 | 123 | + | 2.1 | 154 | + | 2.3 | 130 | − |
| E17 10 | 0.6 | 143 | − | 2.4 | 154 | + | 3.4 | 154 | + | 2.1 | 146 | − |
| 30 | 3.8 | 172 | − | | | | 3.2 | 152 | + | 2.8 | 154 | − |
| E18 23 | 0.7 | 117 | − | 3.0 | 117 | + | 3.4 | 142 | + | 3.3 | 151 | − |
| E19 85 | 0.1 | 165 | − | 2.2 | 119 | + | 2.8 | 150 | + | 1.9 | 152 | − |
| 155 | 3.8 | 14 | − | | | | 3.0 | 150 | + | 1.8 | 150 | − |
| 194 | 3.5 | 179 | − | | | | 3.3 | 153 | + | 1.8 | 152 | − |
| E20 800 | 2.4 | 107 | − | 1.23 | 101 | + | 0.7 | 163 | − | 1.0 | 176 | − |
| 1200 | 1.6 | 98 | − | | | | 1.1 | 166 | − | 1.1 | 176 | − |
| 1800 | 2.8 | 128 | − | | | | 0.8 | 164 | − | 1.3 | 176 | − |
| 2200 | 2.6 | 73 | − | | | | 0.5 | 162 | − | 1.4 | 176 | − |

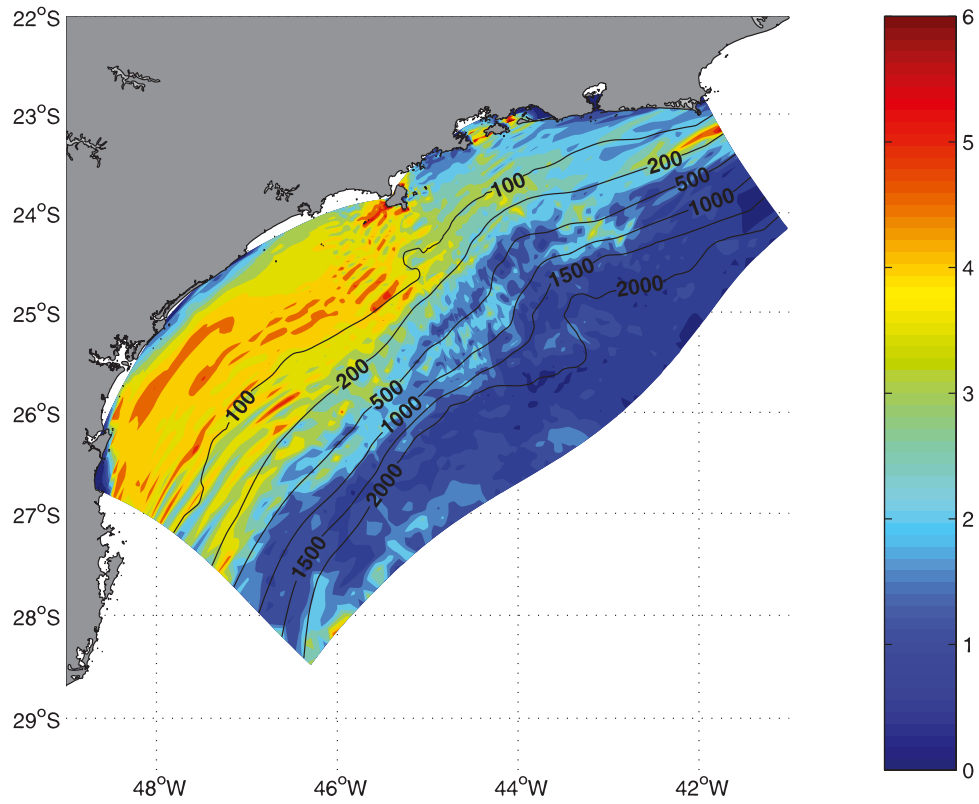[a]For experiment H1, listed values refer to depth-averaged values.

**Figure 7.** RMS $M_2$ baroclinic current (cm s$^{-1}$) from experiment I2 on a near-surface velocity sigma level ($\sigma = -0.00416$). Depth contours are for the 100, 200, 500, 1000, 1500, 2000 and 2500-m isobaths.
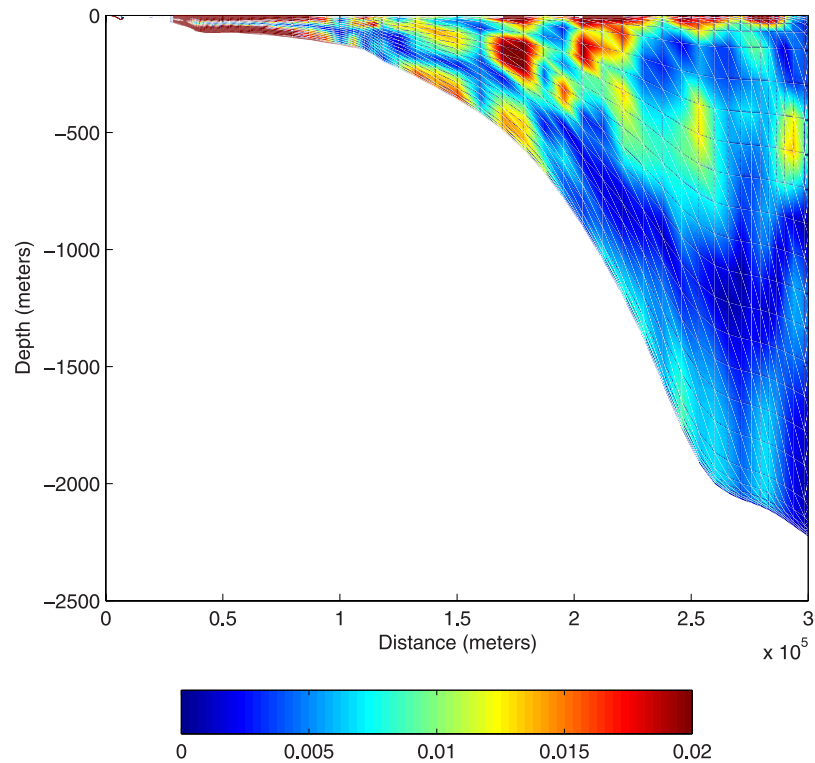


**Figure 8.** Cross-shelf section (see Figure 1) of $M_2$ baroclinic tidal ellipse semi-major axis (m s$^{-1}$) for experiment I2.
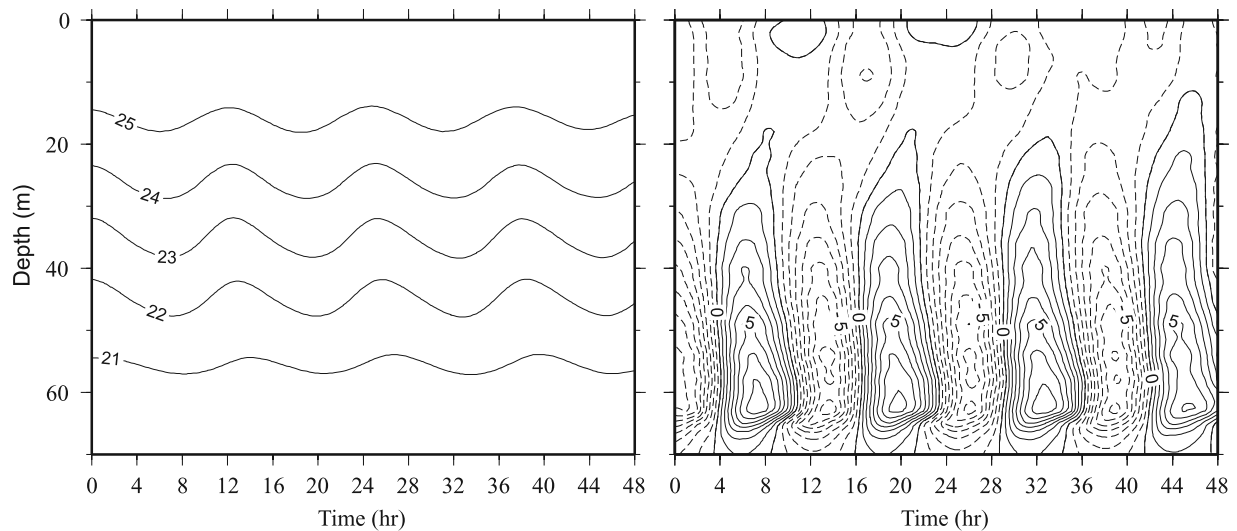
**Figure 9.** Contours of temperature (°C) and $u$ component of velocity field (cm s$^{-1}$) over two tidal cycles at location P1 (see Figure 1) for experiment I2.

Tables 4 and 5). For experiment R3 (I2), RMS differences in the semimajor axis intensity and ellipse inclination are 1.298 cm s$^{-1}$ (1.569 cm s$^{-1}$) and 65.4° (62.4°), respectively. Comparing the observed and modeled direction of rotation of the tidal ellipse in experiment I2, only 39.3% of this comparison is successful as against 90.9% for experiment R3. Differences in the observed and modeled ellipse inclination might be due to inexact bottom topography. In general, comparing ellipse parameters from experiment R3 and observations, the model gives satisfactory results with a few exceptions such as those found at locations C3, H8 and E20. Mooring C3 was deployed

on the slope (see Figure 1) and during the sampling period, two cyclonic BC meanders passed through the area [*Souza*, 2000; *Moreira*, 1997]. Such vortical structures are not represented by the model or in the climatological data set employed to prescribe the initial stratification and, as suggested by the model results presented here, these eddy events may have changed the local mean vertical and horizontal stratification and influenced the baroclinic tidal currents. Differences between the observed and modeled semimajor axes at site H8 may be due to the proximity of the SW open boundary. Site E20 was located just on the NE boundary and a
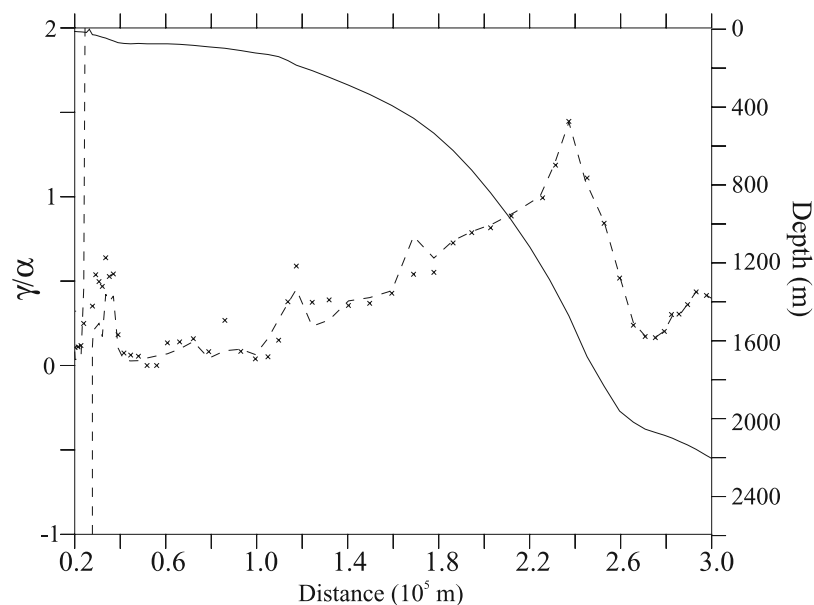


**Figure 10.** Ratio $\gamma/\alpha$ plotted over the bottom topography of the sampled cross-section (see Figure 1) for experiment I2 (symbols) and for experiment R3 (dashed line).
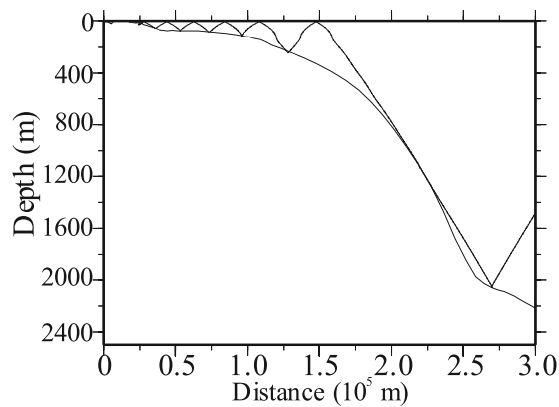
**Figure 11.** Path of the $M_2$ characteristics along the sampled cross-section (see Figure 1) for experiment I2.

comparison was made for a grid point located outside the relaxation zone (section 2.2).

[37] The time mean (over 30 days) vertical eddy diffusivity at a near-bottom sigma level ($\sigma = -0.9916$) for experiment R3 is presented in Figure 17. Following the 100 m and 200 m isobaths and comparing these results with those obtained from calculation I2 (see Figure 12), higher values of $Kd$ are found for experiment R3. Over the shelf close to São Sebastião Island, less intense mixing rates were modeled for experiment R3 but a larger area of the

shelf located to the south has increased $Kd$ values (between $2-3 \times 10^{-4}$). Over the outer shelf, south of São Sebastião Island, $Kd$ values attain $2-3 \times 10^{-4}$ m$^2$ s$^{-1}$ over a larger area than in experiment I2. Maximum mean values ($10 \times 10^{-4}$ m$^2$ s$^{-1}$) found close to the northeastern model boundary are due to the intense vertical shear caused by the BC flow (see Figure 13).

## 4. Discussion and Conclusions

[38] The numerical results indicate that the existence of the BC flowing southward parallel to the shelf break has a strong impact on the baroclinic tidal currents and internal tide activity in the SBB. The interaction with the mean flow reduces the intensity of the baroclinic tidal currents over much of the domain, especially over the shelf and upper slope. Tidal current observations at several points distributed along the shelf did not show internal tide activity everywhere. Further, comparisons between model results and observations were improved when the along-slope flow was considered. These evidences suggest that the results obtained from experiment R3 are more realistic than those from experiment I2.

[39] Nonlinear effects due to vorticity associated with background flows have an important influence upon the propagation of near-inertial internal waves and hence also on mixing [*Davies and Xing*, 2004]. As was shown by *Mooers* [1975], the primary effect of large-scale relative vorticity is to shift the lowest internal wave frequency from
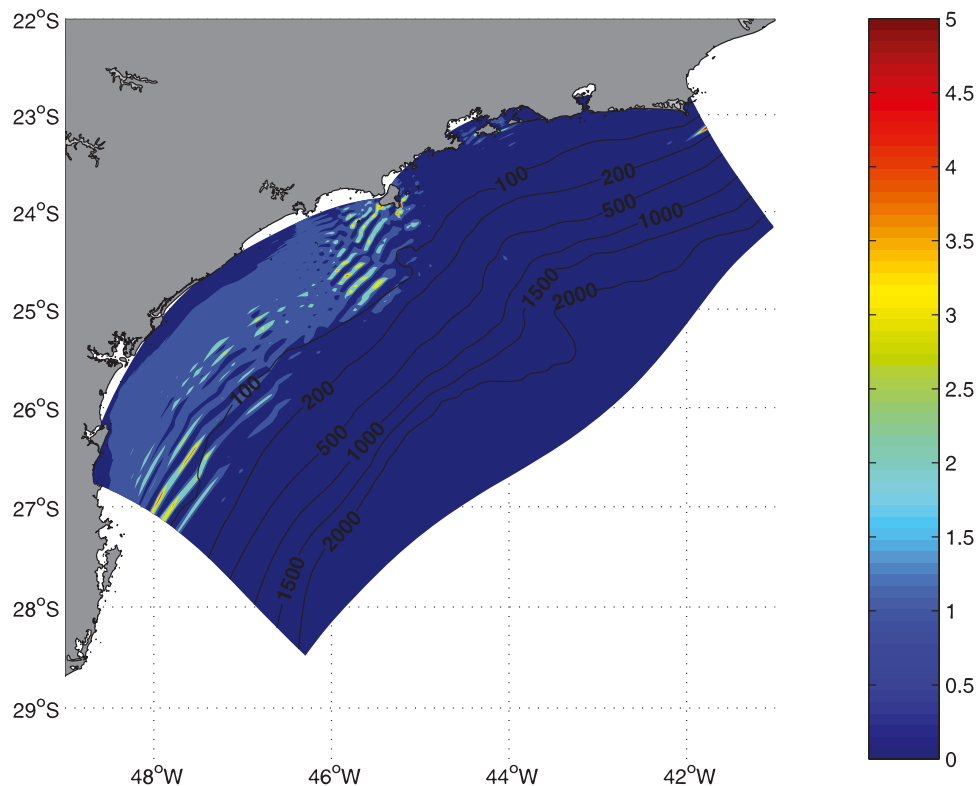


**Figure 12.** Time-mean (over 30 days) eddy diffusivity coefficient ($10^{-4}$ m$^2$ s$^{-1}$) on a near-bottom sigma level ($\sigma = -0.9916$) for experiment I2. Depth contours are for the 100, 200, 500, 1000, 1500, 2000 and 2500-m isobaths.
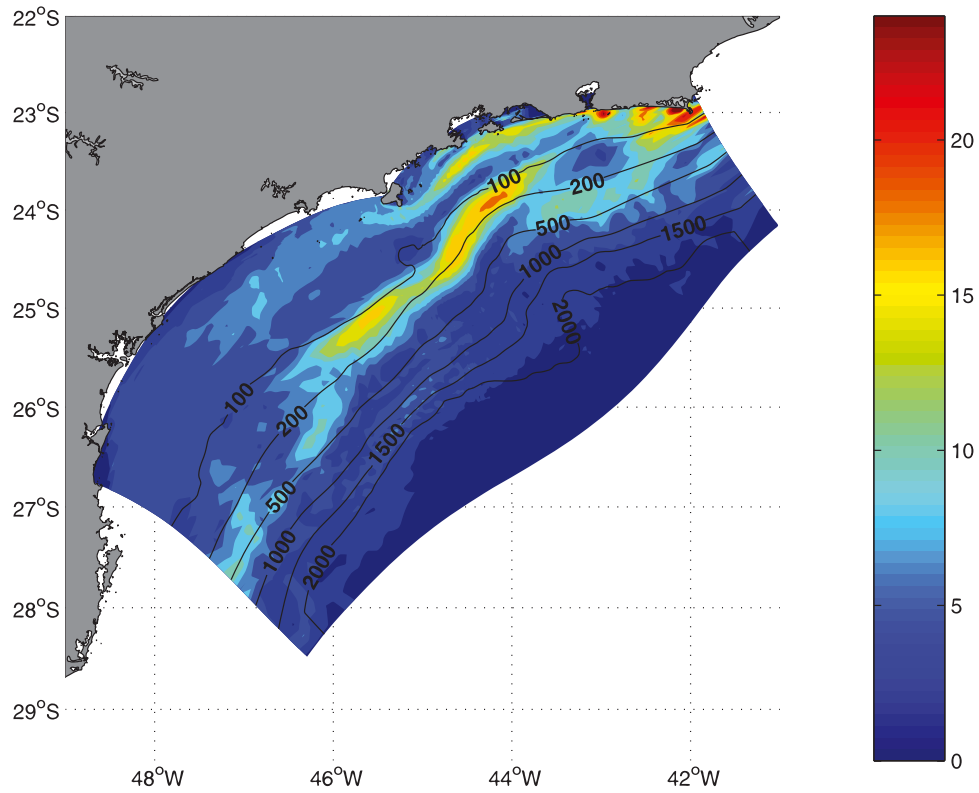
**Figure 13.** RMS baroclinic currents (cm s$^{-1}$) with subinertial frequencies from experiment R3 on a near-surface velocity sigma level ($\sigma = -0.00416$). Depth contours are for the 100, 200, 500, 1000, 1500, 2000 and 2500-m isobaths.
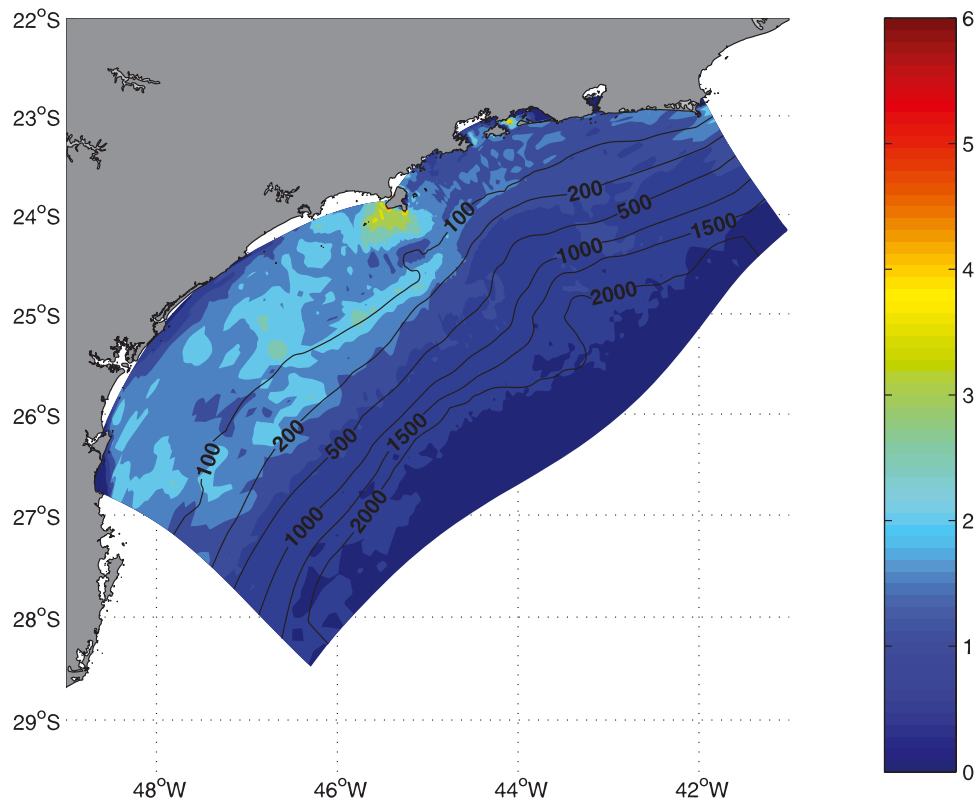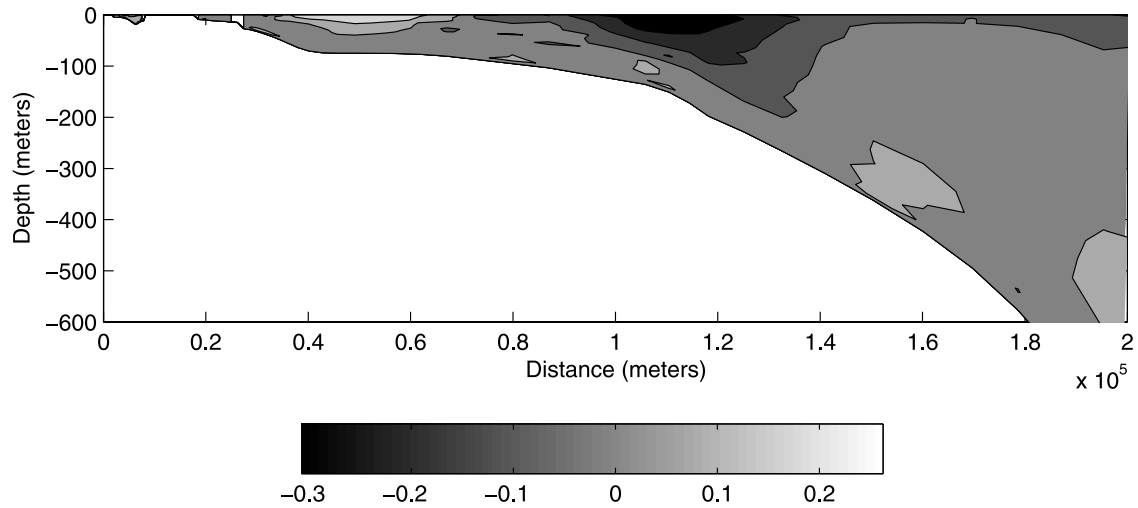


**Figure 14.** Rms baroclinic currents (cm s$^{-1}$) with superinertial frequencies from experiment R3 on a near-surface velocity sigma level ($\sigma = -0.00416$). Depth contours are for the 100, 200, 500, 1000, 1500, 2000 and 2500-m isobaths.

**Figure 15.** Instantaneous along-slope velocity (m s$^{-1}$) 45 days after initialization. Negative values indicate southward flow.

the Coriolis frequency $f$ to an effective Coriolis frequency $f_{eff}(x, y, t) = f + 0.5\zeta(x, y, t)$ where $\zeta = (\partial V/\partial x) - (\partial U/\partial y)$ is the low-frequency ($\sigma < 0.73$ *cpd*) vertical vorticity of the medium. Such a shift creates waveguide conditions in the regions of negative relative vorticity that may lead to the trapping of near-inertial waves [*Mooers*, 1975] and concentration of near-inertial energy due to diminishing group velocity [*Kunze*, 1985].

[40] The coastal side of the BC has negative vorticity. Figure 18 shows $f_{eff}$ values during 5 days at a near-surface sigma level ($\sigma = -0.00416$) at the cross-shelf slice indicated in Figure 1 between the 70 m and 250 m isobaths. In general, along the 100 m isobath (Figure 18, dashed line), $f_{eff} < \omega_{M2}$ ($\omega_{M2} = 1.40518 \times 10^{-4}$ s$^{-1}$), but during some periods (e.g., of from 70 to 80 hours), $f_{eff} > \omega_{M2}$ or $f_{eff}$ becomes very close to $\omega_{M2}$. Hence internal wave generation
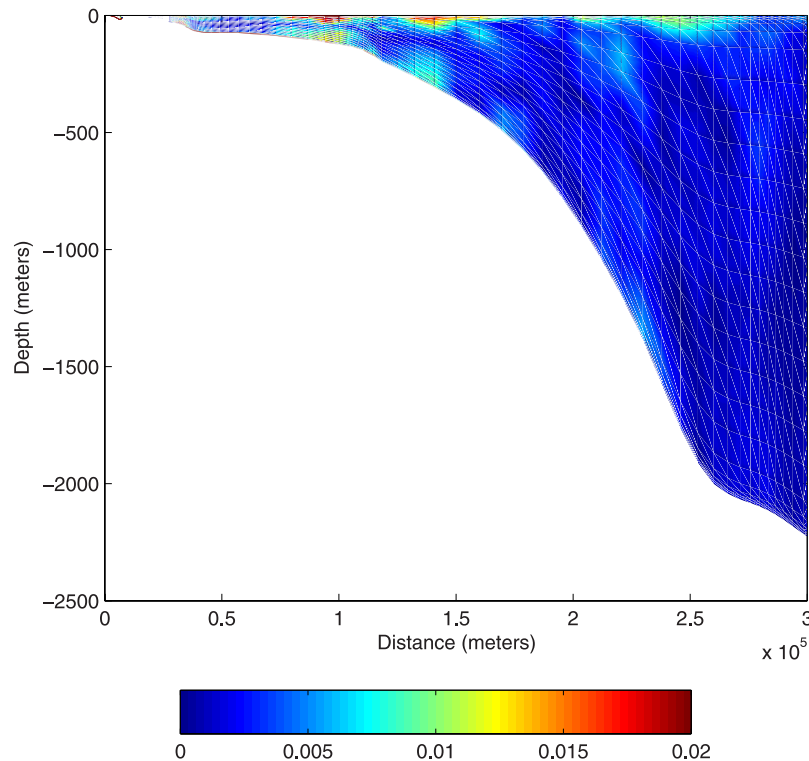


**Figure 16.** Cross-shelf section (see Figure 1) of M$_2$ baroclinic tidal ellipse semi-major axis (m s$^{-1}$) for experiment R3.
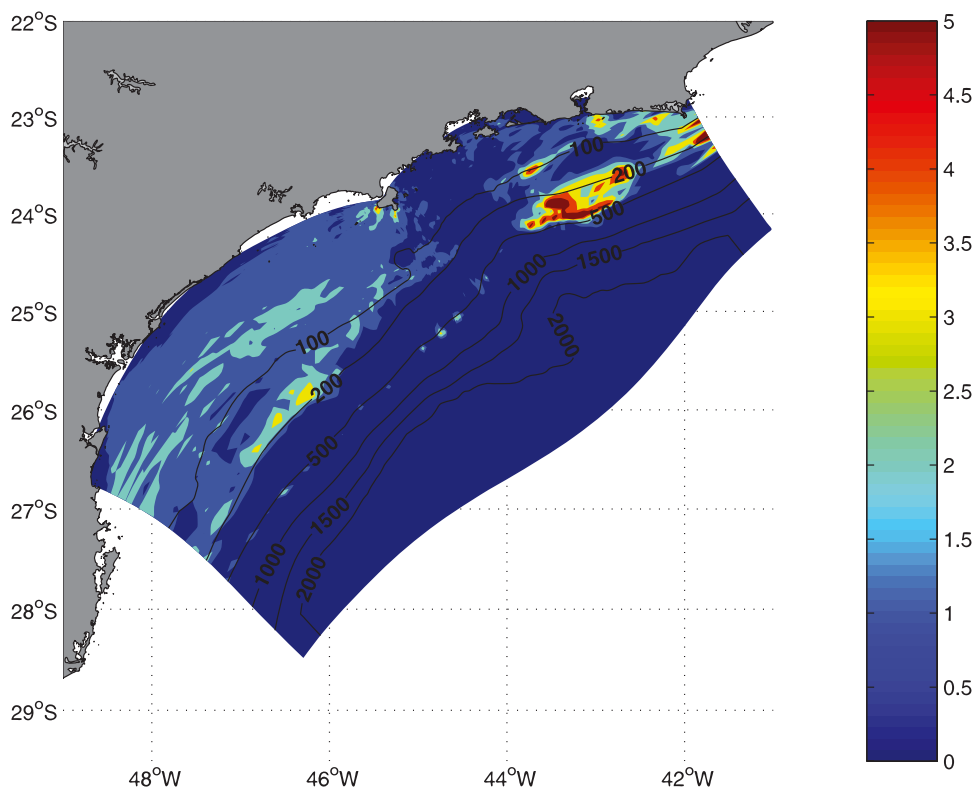
**Figure 17.** Time-mean (over 30 days) eddy diffusivity coefficient ($10^{-4}$ m$^2$ s$^{-1}$) on a near-bottom sigma level ($\sigma = -0.9916$) for experiment R3. Depth contours are for the 100, 200, 500, 1000, 1500, 2000 and 2500-m isobaths.

on this side of the BC at a subinertial frequency cannot propagate horizontally, although vertical propagation is possible, giving a region of enhanced variance with depth [*Davies and Xing*, 2004].

[41] Equation (1) incorporates the current shear effect due to background flows replacing $f$ by $f_{eff}$. Figure 19 shows internal tide characteristics calculated considering the vorticity for a moment when $f_{eff} > \omega_{M2}$ (75 hours in Figure 18). In this case, there is no internal tide propagation to the shelf. The vorticity thus has the theoretical potential to increase $f_{eff}$ sufficiently to reflect, trap or prohibit the generation of the M$_2$ internal tide. This may explain the reduced modeled internal tide signal over the shelf in experiment R3 as compared to that in experiment I2 and the high baroclinic M$_2$ velocities modeled close to the coastal front of the BC. These results suggest that at a fixed point in space, the internal tide signal may therefore inevitably appear as intermittent, governed by the timescale of the motions that modulate the vorticity. *Shcherbina et al.* [2003] also found a local intensification of the downward energy flux consistent with the trapping of near-inertial waves by the region of negative relative vorticity associated with the subpolar front in the Japan Sea.

[42] On the positive vorticity side ($\approx$200 m), M$_2$ internal tides are superinertial (Figure 18, dotted line). Since their frequency lies in the range $f_{eff} < \omega_{M2} < N$, they will propagate outside the region [*Mooers*, 1975; *Kunze*, 1985]. In the case of experiment R3, a plausible explanation for the generation and propagation of the internal tide seems to be that they are generated over

the upper slope and propagated coastwards ($\gamma < \alpha$, Figure 10), being reflected by the positive vorticity region of the BC. After reflection, they propagated seawards,
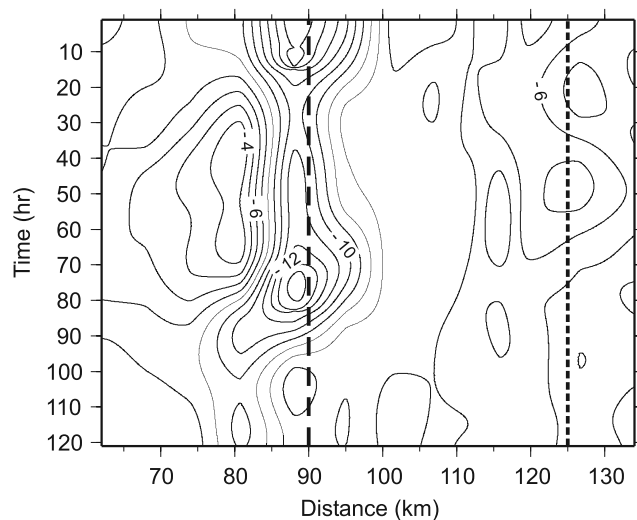


**Figure 18.** Contours of low-pass filtered (frequencies < 0.75 cpd) effective inertial frequency $f_{eff}$ ($10^{-5}$ s$^{-1}$) on a near-surface sigma level ($\sigma = -0.0416$) over 5 days along the sample cross-slice (see Figure 1) between 70 m and 350 m. Contour interval is $2 \times 10^{-5}$ s$^{-1}$. The dashed and dotted lines indicate the position of the 100 m and 200 m isobaths, respectively.
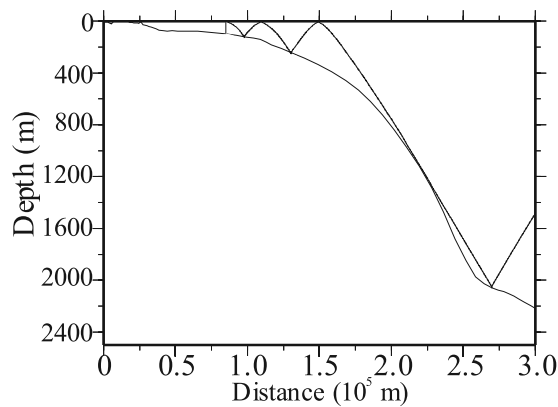
**Figure 19.** Path of the M$_2$ characteristics along the sampled cross-section (see Figure 1) for experiment R3. These characteristics were computed replacing $f$ by $f_{eff}$ at time = 75 h (Figure 18) on equation (1).

giving rise to the surface semimajor axis maximum at x $\approx$ 2.5 $\times$ 10$^5$ m (Figure 16).

[43] The trapping of the internal tide, along the negative vorticity side of the BC, and its reflection, along the positive side, together with the increased vertical shear promoted by the BC flow itself are responsible for the enhanced turbulence and mixing modeled along the 100 m and 200 m isobaths. *Davies and Xing* [2004] found similar results when investigating the frontal influence upon wind-induced internal wave generation and propagation.

[44] Another point that deserves some discussion is the impact of the BC's meandering and eddies upon internal tides along the SBB. The BC presents intense meandering and eddy activity as it flows along the SBB [*Silveira et al.*, 2004], modifying not only the horizontal and vertical stratification due to shelf break up- and downwelling [*Campos et al.*, 1999], but also changing the relative vorticity field [*Godoi*, 2005]. Although such meso-scale processes were not considered in the numerical simulations presented here, it is clear, from the results obtained, that they may have a strong impact on the internal tide field and tidally induced mixing on both temporal and spatial scales.

[45] The results presented in this paper suggest that in regions of strong baroclinic flows, internal tides may not be investigated independently of the background flows if the internal tide field and associated mixing are to be properly accounted for. Diurnal internal tides at mid latitudes may be more greatly affected by the mean flow than are the internal tides with semidiurnal period because their frequency is closer to the inertial frequency at this latitude range. As pointed out by *Hosegood* [2005], theoretical and modelling studies of internal tide generation and propagation do not generally account for temporal variability in background conditions. However, as shown here, to omit it is to ignore a process that may, in the real ocean, completely overwhelm internal tide behaviour. Hence the dynamic and complex interaction of flows on the slope and their broad range of temporal and spatial scales present great challenges if one is fully to understand the slope region and to assess its relevance to global mixing in addition to the local processes which impact sediment transport and the plankton and benthic community.

## References

Alves, M. A. (1992), Correntes de maré e inerciais na plataforma continental ao largo de Ubatuba, Master's thesis, 162 pp., Univ. de São Paulo, São Paulo, Brazil.

Azevedo, A., J. C. B. da Silva, and A. L. New (2006), On the generation and propagation of internal solitary waves in the southern Bay of Biscay, *Deep Sea Res.*, 53, 927–941.

Baines, P. G. (1973), The generation of internal tides by flat-bump topography, *Deep Sea Res.*, 20, 179–205.

Baines, P. G. (1982), On internal tide generation models, *Deep Sea Res., Part A*, 29, 307–338.

Blumberg, A. F., and G. L. Mellor (1987), A description of a three-dimensional coastal ocean circulation model, in *Three-Dimensional Coastal Ocean Models, Coastal Estuarine Stud.*, vol. 4, edited by N. Heaps, pp. 1–16, AGU, Washington, D. C.

Campos, E. J., D. Velhote, and I. C. da Silveira (1999), Shelf break upwelling driven by Brazil Current cyclonic meanders, *Geophys. Res. Lett.*, 26, 2061–2064.

Castro, B. M., and L. B. Miranda (1998), Physical oceanography of the western Atlantic continental shelf located between 4°N and 34°S, in *The Sea*, vol. 11, edited by A. R. Robinson and K. H. Brink, pp. 209–251, John Wiley, Hoboken, N. J.

Chapman, D. C. (1985), Numerical treatment of cross-shelf open boundaries in a barotropic coastal ocean model, *J. Phys. Oceanogr.*, 15, 1060–1075.

Cheng, C. (1992), Variability of currents in Great South Channel and over Georges Bank: observations and modeling, *Rep. WHOI-92-20*, 288 pp., Woods Hole Oceanogr. Inst., Woods Hole, Mass.

Cummins, P. F., and L.-Y. Oey (1997), Simulation of barotropic and baroclinic tides off northern British Columbia, *J. Phys. Oceanogr.*, 27, 762–781.

Davies, A. M., and J. Xing (2004), Modelling processes influencing wind-induced internal wave generation and propagation, *Cont. Shelf Res.*, 24, 2245–2271.

Egbert, G. D., and S. Erofeeva (2002), Efficient inverse modeling of barotropic ocean tides, *J. Atmos. Oceanic Technol.*, 19, 183–204.

Foreman, M. G. G. (1977), Manual for tidal height analysis and prediction, *Pac. Mar. Sci. Rep. 77-10*, 97 pp., Inst. of Ocean Sci., Victoria, B.C., Canada.

Foreman, M. G. G. (1978), Manual for tidal current analysis and prediction, *Pac. Mar. Sci. Rep. 78-6*, 70 pp., Inst. of Ocean Sci., Victoria, B.C., Canada.

Fundação de Estudos do Mar (FEMAR) (2000), Catálago de Estacões Maregráficas Brasileiras, edited by F. J. P. Salles, F. C. M. Bentes, and J. A. Santos, 280 pp., Rio de Janeiro, Brazil.

Gerkema, T. (1996), A unified model for the generation and fission of internal tides in a rotating ocean, *J. Mar. Res.*, 54, 421–450.

Godoi, S. S. (2005), Dinâmica quase-geostrófica do Sistema Corrente do Brasil no Embaiamento de São Paulo, Ph.D. thesis, 133 pp., Univ. de São Paulo, São Paulo, Brazil.

Haney, R. (1991), On the pressure gradient force over steep topography in sigma coordinate ocean models, *J. Phys. Oceanogr.*, 21, 610–619.

Holloway, P. E. (2001), A regional model of the semidiurnal internal tide on the Australian North West Shelf, *J. Geophys. Res.*, 106, 19,625–19,638.

Hosegood, P. (2005), Observations of the impact of flow-topography interactions on mixing processes within a confined basin: the Faeroe Shetland Channel, Ph.D. thesis, 213 pp., Univ. van Utrecht, Utrecht, Netherlands.

Huthnance, J. M. (1989), Internal tides and waves near the continental shelf edge, *Geophys. Astrophys. Fluid Dyn.*, 48, 81–106.

Kunze, E. (1985), Near-inertial wave propagation in geostrophic shear, *J. Phys. Oceanogr.*, 15, 544–565.

Ledwell, J. R., E. T. Montgomery, K. L. Polzin, L. C. St. Laurent, R. W. Schmitt, and J. M. Toole (2000), Evidence for enhanced mixing over rough topography in the abyssal ocean, *Nature*, 403, 179–182.

Mellor, G. L. (1996), User's guide for a three-dimensional, primitive equation, numerical ocean model, 35 pp., Atmos. and Oceanic Sci. Program, Princeton Univ., Princeton, N. J.

Mellor, G. L., and T. Yamada (1982), Development of a turbulent closure model for geophysical fluid problem, *Rev. Geophys.*, 20, 851–875.

Mesquitade, A. R., and J. Harari (2003), On the harmonic constants of tides and tidal currents of the south-eastern Brazilian shelf, *Cont. Shelf Res.*, 23, 1227–1237.

Miranda, L. B. (1982), Análise de massas de água da plataforma continental e da região oceânica adjacente: Cabo de São Tomé (RJ) à Ilha de São Sebastião (SP), Livre-Docente thesis, 194 pp., Univ. de São Paulo, São Paulo, Brazil.

Mooers, C. N. K. (1975), Several effects of a baroclinic current on the cross-stream propagation of inertial-internal waves, *Geophys. Fluid Dyn.*, *6*, 245–275.

Moreira, J. R. G. B., (1997), Correntes na plataforma externa e talude ao largo de Santos: observa cões no verão de 1993, Master's thesis, 214 pp., Univ. de São Paulo, São Paulo, Brazil.

Munk, W. H., and C. Wunsch (1998), Abyssal recipes II: energetics of tidal and wind mixing, *Deep Sea Res.*, *45*, 1977–2000.

Nash, J. D., E. Kunze, J. M. Toole, and R. W. Schmitt (2004), Internal tide reflection and turbulent mixing on the continental slope, *J. Phys. Oceanogr.*, *34*, 1117–1134.

Pereira, A. F., and B. M. Castro (2007), Internal tides in the southwestern Atlantic off Brazil: observations and numerical modeling, *J. Phys. Oceanogr*, in press.

Pereira, A. F., A. L. Belém, B. M. Castro, and R. Geremias (2005), Tide-topography interaction along the eastern Brazilian shelf, *Cont. Shelf Res.*, *25*, 1521–1539.

Polzin, K. L., J. M. Toole, J. R. Ledwell, and R. W. Schmitt (1997), Spatial variability of turbulent mixing in the abyssal ocean, *Science*, *276*, 93–96.

Puig, P., A. Palanques, J. Guillén, and M. El Khatab (2004), Role of internal waves in the generation of nepheloid layers on the northwestern Alboran slope: implications for continental shelf shaping, *J. Geophys. Res.*, *109*, C09011, doi:10.1029/2004JC002394.

Rainville, L., and R. Pinkel (2004), Observations of energetic high-wavenumber internal waves in the Kuroshio, *J. Phys. Oceanogr.*, *34*, 1495–1505.

Rattray, M., J. G. Dworski, and P. E. Kovala (1969), Generation of long internal waves at the continental slope, *Deep Sea Res.*, *16*, 179–195.

Rezende, J. H. M. (2003), Intrusões da Água Central do Atlântico Sul na plataforma continental sudeste durante o verão, Ph.D. thesis, 120 pp., Univ. de São Paulo, São Paulo, Brazil.

Sandstrom, H. (1976), On topographic generation and coupling of internal waves, *Geophys. Fluid Dyn.*, *7*, 231–270.

Schwiderski, E. W. (1980), On charting global ocean tides, *Rev. Geophys.*, *18*, 243–268.

Shcherbina, A. Y., L. D. Talley, E. Firing, and P. Hacker (2003), Near-surface frontal zone trapping and deep upward propagation of internal wave energy in the Japan/East Sea, *J. Phys. Oceanogr.*, *33*, 900–912.

Silveira, I. C. A., W. S. Brown, and G. R. Flierl (2000), Dynamics of the North Brazil Current retroflection region from the WESTRAX observations, *J. Geophys. Res.*, *105*(C12), 28,559–28,584.

Silveira, I. C. A., L. Calado, B. M. Castro, M. Cirano, J. A. M. Lima, and A. S. Mascarenhas Jr. (2004), On the baroclinic structure of the Brazil Current Intermediate Western Boundary Current System, *Geophys. Res. Lett.*, *31*, L14308, doi:10.1029/2004GL020036.

Smagorinsky, J. S. (1963), General circulation experiments with primitive equations: I. The basic experiment, *Mon. Weather Rev.*, *91*, 99–164.

Souza, M. C. A. (2000), A Corrente do Brasil ao largo de Santos: medições diretas, Master's thesis, 169 pp., Univ. de São Paulo, São Paulo, Brazil.

van Haren, H. (2004), Incoherent internal tidal currents in the deep ocean, *Ocean Dyn.*, *54*, 66–76.

Wunsch, C. (1975), Internal tides in the ocean, *Rev. Geophys.*, *13*, 167–182.

Xing, J., and A. M. Davies (1998), A three-dimensional model of internal tides on the Malin-Hebrides shelf and shelf edge, *J. Geophys. Res.*, *103*, 27,821–27,847.

————————————

L. Calado, B. M. Castro, A. F. Pereira, and I. C. A. da Silveira, Departamento de Oceanografia Física, Química e Geológica, Instituto Oceanográfico, Universidade de São Paulo, Praça do Oceanográfico 191 Cidade Universitária, São Paulo, SP 05508-900, Brazil. (afpereira2002@yahoo.com.br)